ELSEVIER

Self-consistent modeling of large plastic deformation, texture and morphology evolution in semi-crystalline polymers

S. Nikolov[a,*], R.A. Lebensohn[b], D. Raabe[a]

[a]*Max-Planck-Institut für Eisenforschung, Max-Planck-Str. 1, 40237 Düsseldorf, Germany*
[b]*Los Alamos National Laboratory, Los Alamos, NM 87545, USA*

Abstract

A self-consistent model for semi-crystalline polymers is proposed to study their constitutive behavior, texture and morphology evolution during large plastic deformation. The material is considered as an aggregate of composite inclusions, each representing a stack of crystalline lamellae with their adjacent amorphous layers. The deformation within the inclusions is volume-averaged over the phases. The interlamellar shear is modeled as an additional slip system with a slip direction depending on the inclusion's stress. Hardening of the amorphous phase due to molecular orientation and, eventually, coarse slip, is introduced via Arruda–Boyce hardening law for the corresponding plastic resistance. The morphology evolution is accounted for through the change of shape of the inclusions under the applied deformation gradient. The overall behavior is obtained via a viscoplastic tangent self-consistent scheme. The model is applied to high density polyethylene (HDPE). The stress–strain response, texture and morphology changes are simulated under different modes of straining and compared to experimental data as well as to the predictions of other models.
© 2006 Elsevier Ltd. All rights reserved.

---

*Corresponding author. Tel.: +49 211 6792 260; fax: +49 211 6792 333.
  E-mail address: nikolov@mpie.de (S. Nikolov).

1. Introduction

Semi-crystalline polymers are increasingly used in structural applications where the influence of the microstructure and its evolution on the macroscopic mechanical properties is of prime importance. A number of applications, such as thin films, coatings, high-modulus fibers and ribbons, display highly anisotropic mechanical and crystallographic properties and their processing often involves large plastic deformation of an initially isotropic material.

The microstructure of melt-crystallized polymers consists of broad, thin crystalline lamellae separated by amorphous layers. Locally, the lamellae are grown from a central nucleus and are radially oriented, which results in the formation of spherulitic structures (e.g. Lin and Argon, 1994). During large plastic deformation, profound changes in both the crystallographic texture and morphology take place. It has been observed (e.g. Butler et al., 1998; Hiss et al., 1999) that in uniaxial tension of HDPE, the initial lamellar microstructure is gradually destroyed and replaced by stretched fibrils (Fig. 1). Similar lamellar-to-fibrillar transition processes have also been reported from simple-shear experiments of HDPE (Bartczak et al., 1994).

In the past fifteen years, several micromechanical models have been developed in order to simulate the stress–strain behavior and crystallographic texture evolution in semi-crystalline polymers at large strains. Parks and Ahzi (1990) proposed a purely crystalline model treating the lack of five independent slip systems in polymer crystals. Ahzi et al. (1990) developed a bi-crystal approach, where the basic structural unit of semi-crystalline polymers was introduced as a two-phase composite inclusion consisting of a single, flat
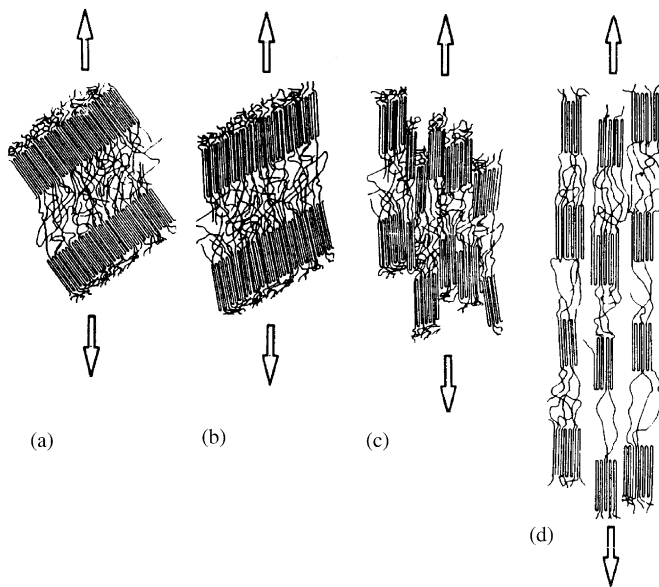
Fig. 1. Morphology change during lamellae stack deformation in a tensile test, after Schultz (1974): (a) interlamellar shear; (b) interlamellar shear plus fine slip in the crystals; (c) coarse slip plus initiation of lamellae breakage; (d) fibrillar state with residual crystalline block portions. Arrows show the loading direction. The imposed deformation increases from left to right.

lamella and its adjacent amorphous layer (Fig. 2a). Both models used Taylor's assumption for the overall properties. This approach yields a very stiff stress–strain response and overestimates the rate of the texture evolution. Dahoun et al. (1991) represented the crystalline polymer as an aggregate of crystalline lamellae in the form of oblate ellipsoids. The average properties have been found via a tangent self-consistent scheme. Due to the more realistic modeling of the interactions between the crystals, the obtained results agreed reasonably well with the experiments despite the fact that the amorphous phase contribution was not considered. Later, Lee et al. (1993a) used the composite inclusion depicted in Fig. 2a, coupled with Sachs- and self-consistent-like interaction laws. The model produced valuable results about the stress–strain behavior and crystallographic texture development of HDPE. Recently, van Dommelen et al. (2003) extended the rigid-viscoplastic modeling of Lee et al. (1993a) to elasto–viscoplastic behavior using a deformation gradient formulation and the same composite inclusion model. With this approach they were able to simulate cyclic loadings of semi-crystalline polymers.

Despite the above mentioned efforts, many important phenomena related to the strain-induced evolution of the microstructure are not fully accounted for in the existing models. For example, there were no attempts to incorporate the strain localization within the crystals and their subsequent fragmentation into smaller blocks, the strain-induced decrease in crystallinity (Raabe et al., 2004) or the transformation of the morphology from a lamellar to a fibrillar state (Fig. 1). Undoubtedly, all of these microscopic processes influence the macroscopic mechanical properties and their integration into the constitutive modeling should result in better predictions of the observed stress–strain response and texture evolution.

In the present work, we develop a micromechanical model which, besides the stress–strain behavior and the crystallographic texture evolution, also takes into account the morphology evolution of the microstructure. We restrict our attention to monotonic loadings. The material is assumed to be incompressible. For the sake of simplicity, elasticity is neglected, which is a reasonable approximation for highly crystalline polymers and polymers with glassy amorphous phase where the purely elastic strain does not exceed 3%. Following Lee et al. (1993a), we ignore the radial arrangement of the lamellae in the spherulites and use a basic structural unit representing only a part of a spherulite. This
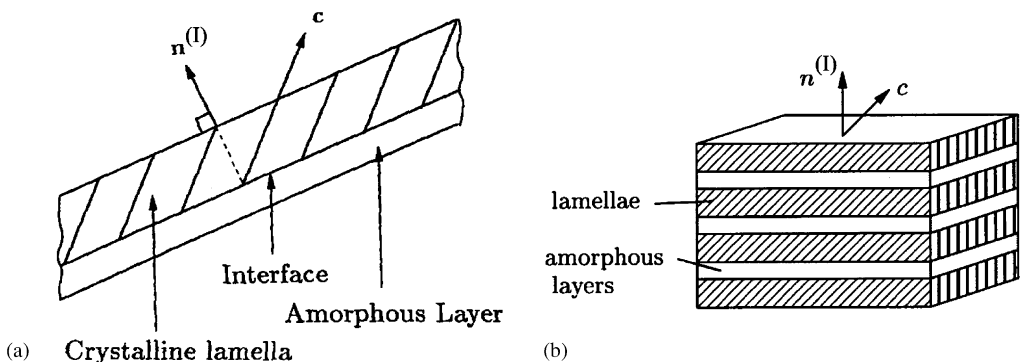
Fig. 2. The basic structural unit of a semi-crystalline polymer: (a) composite plane inclusion, after Lee et al. (1993a); (b) lamellae stack inclusion, after Nikolov and Doghri (2000); $\mathbf{n}^{(I)}$—normal to the lamella(e)/amorphous layer(s) interface; $\mathbf{c}$—chain direction in the crystals.

simplification is motivated by the fact that, despite some efforts in this direction, the influence of the spherulitic structure as such on the macroscopic mechanical properties has not been proven experimentally. Moreover, at large deformations the spherulites are gradually destroyed (Bartczak et al., 1992a). With these considerations in mind, here we assume that an aggregate consisting of randomly oriented composite inclusions, which are smaller than the spherulites, behaves in the same way as an aggregate where the inclusions are arranged in spherulitic-like structures as long as the macroscopic mechanical properties are concerned. In contrast to the inclusion model used by Lee et al. (1993a), we define the basic structural unit of semi-crystalline polymers as a stack of crystalline lamellae with their adjacent amorphous layers according to Fig. 2b (Nikolov and Doghri, 2000). This choice is motivated by several reasons. Firstly, the composite plane inclusion from Fig. 2a, is a nearly 2D object, which makes it difficult to introduce its shape in the model. Hence, the self consistency conditions for the aggregate should be explicitly based on the equilibrium and compatibility conditions at the crystalline/amorphous interfaces instead of the inclusions' boundaries. Given that during coarse slip the interfaces are destroyed (see Fig. 1), the latter self consistency conditions are not a natural choice. Thirdly, the lamellae stack inclusion seems to better reflect the physical reality. Experimental observations have shown that during deformation, stacks of several parallel lamellae rotate as a rigid body (e.g. Lin and Argon, 1994). The formation of lamellae stacks is due to the fact that many of the polymer chains forming the crystals run through several neighboring lamellae, thus creating tie molecules and loose loops that link several lamellae together. At the crystalline/amorphous interface, the lamellae normals, $\mathbf{n}^{(I)}$, are assumed to be tilted at a certain angle with respect to the direction of the polymer chains in the crystals, $\mathbf{c}$ (Fig. 2), as observed experimentally (Bassett and Hodge, 1981).

The definition of the composite inclusion as a lamellae stack allows us to incorporate its shape and strain-induced transformation into the micromechanical modeling. In our model, the change of the inclusion's shape under the action of the local deformation gradient represents the morphology evolution. The average behavior of the aggregate is obtained by including the lamellae-stack inclusion model into a viscoplastic tangent self-consistent scheme. This homogenization procedure was proposed by Molinari et al. (1987) and generalized by Lebensohn and Tomé (1993) for anisotropic polycrystals and arbitrary ellipsoidal shape of the inclusions. With this approach, the relatively soft interactions between the lamellae stacks are modeled in a realistic way. Moreover, both local equilibrium and compatibility between a given inclusion and its surrounding are satisfied.

Finally, it is worth mentioning that the use of a lamellar structure as the basic unit in the context of a self-consistent formulation was also successfully applied to the study of the mechanical properties and texture evolution of an intermetallic Ti–Al aggregate consisting of multiple lamellar colonies (i.e., polysynthetic twins) (Lebensohn, 1999).

The article is organized as follows: First, we describe the constitutive relations for the different phases and the composite inclusion. Next, we outline the averaging scheme and the methods for texture and morphology update. Finally, we apply the micromechanical model to HDPE subjected to uniaxial tension, uniaxial compression and simple shear. The obtained results are compared to experimental stress–strain and texture data as well as to the simulation results reported in Lee et al. (1993b). Notation conventions are as follows: Scalars are in mathematical italics, boldface symbols are used for tensors, the order of

which is indicated by the context. Dots and colons indicate tensor products contracted over one and two indices, respectively, e.g.,

$$(\mathbf{A} \cdot \mathbf{B})_{ij} = A_{ij}B_{kj}; \quad (\mathbf{C} : \mathbf{D})_{ijkl} = C_{ijmn}D_{nmkl}.$$

Dyadic tensor products are designated by $\otimes$, e.g.,

$$(\mathbf{a} \otimes \mathbf{b})_{ij} = a_i b_j; \quad (\mathbf{A} \otimes \mathbf{B})_{ijkl} = A_{ij}B_{kl}.$$

The second- and fourth-order identity tensors are denoted as $\mathbf{1} \equiv \delta_{ij}$ and $\mathbf{I} \equiv I_{ijkl} = \frac{1}{2}(\delta_{ik}\delta_{jl} + \delta_{il}\delta_{jk})$, respectively. The inverse and the transpose of a matrix $\mathbf{C}$ are indicated by $\mathbf{C}^{-1}$ and $\mathbf{C}^{\mathrm{T}}$, respectively.

2. Constitutive relations

2.1. Crystalline phase

Polymer crystals are formed by folding and association of long polymer molecules. Plastic deformation proceeds mainly via crystallographic slip on a limited number of planes (e.g. G'Sell and Dahoun, 1994). Thus, despite the physical differences with respect to the small-molecules crystals, they can be conveniently modeled with the same basic equations used for metals and other crystalline materials. A distinctive feature of the polymer crystals is that a single polymer crystal cannot accommodate a general macroscopic deformation because it lacks five independent slip systems due to the inextensibility of the polymer chains in the chain direction (Lee et al., 1993a). For example, the orthorhombic polyethylene crystals considered here possess only four independent slip systems. We do not consider this kinematic deficiency further because the self-consistent approach does not require any special treatment of low-symmetry single crystals.

The velocity gradient $\mathbf{L}_c^p$ in the crystalline lamellae due to plastic deformation (without rigid rotation) is defined as the sum of the shear rates $\dot{\gamma}_\alpha$ over all distinct slip systems (α):

$$\mathbf{L}_c^p = \sum_\alpha \dot{\gamma}_\alpha (\mathbf{b}^{(\alpha)} \otimes \mathbf{n}^{(\alpha)}), \tag{1}$$

where the unit vectors $\mathbf{b}^{(\alpha)}$ and $\mathbf{n}^{(\alpha)}$ denote the slip direction and the normal to the slip plane (α), respectively.

Further, $\mathbf{L}_c^p$ can be split into symmetric and asymmetric parts as follows:

$$\mathbf{L}_c^p = \mathbf{D}_c^p + \mathbf{W}_c^p,$$
$$\mathbf{D}_c^p = \sum_\alpha \frac{\dot{\gamma}_\alpha}{2}(\mathbf{b}^{(\alpha)} \otimes \mathbf{n}^{(\alpha)} + \mathbf{n}^{(\alpha)} \otimes \mathbf{b}^{(\alpha)}) \equiv \sum_\alpha \dot{\gamma}_\alpha \mathbf{R}^{(\alpha)},$$
$$\mathbf{W}_c^p = \sum_\alpha \frac{\dot{\gamma}_\alpha}{2}(\mathbf{b}^{(\alpha)} \otimes \mathbf{n}^{(\alpha)} - \mathbf{n}^{(\alpha)} \otimes \mathbf{b}^{(\alpha)}) \equiv \sum_\alpha \dot{\gamma}_\alpha \mathbf{A}^{(\alpha)}, \tag{2}$$

where $\mathbf{D}_c^p$ and $\mathbf{W}_c^p$ denote the plastic rate of deformation and the spin caused by plastic deformation, respectively; $\mathbf{R}^{(\alpha)}$ and $\mathbf{A}^{(\alpha)}$ are the symmetric and the asymmetric Schmid tensors, respectively.

The resolved shear stress τ_α acting on a slip system (α) can be found from the deviatoric part, $\mathbf{s}_c$, of the Cauchy stress $\boldsymbol{\sigma}_c$ as:

$$\tau_\alpha = \mathbf{s}_c : \mathbf{R}^{(\alpha)}, \tag{3}$$

where $\mathbf{s}_c \equiv \boldsymbol{\sigma}_c - \frac{1}{3}\mathrm{tr}(\boldsymbol{\sigma}_c)\mathbf{1}$.

The microscopic shear rate on (α) is related to τ_α by a nonlinear power law (e.g. Asaro and Needleman, 1985):

$$\dot{\gamma}_\alpha = \dot{\gamma}_0 \frac{\tau_\alpha}{g_\alpha}\left|\frac{\tau_\alpha}{g_\alpha}\right|^{n_c-1} \quad \text{(no sum)}, \tag{4}$$

where $\dot{\gamma}_0$ is a reference strain rate, $g_\alpha > 0$ is the shear resistance of the slip system (α) and $n_c = 1/m_c$ denotes the inverse of the crystals' rate sensitivity m_c. Because of the low lamellae thickness, strain-induced hardening of the resistances, g_α, is neglected.

The crystallographic slip in the lamellae can be divided into two groups, namely, *chain slip* with slip direction along $\mathbf{c}$ (Fig. 2), and *transverse slip* with direction perpendicular to $\mathbf{c}$. On the other hand, the deformation can proceed via a quasi-homogeneous mode (*fine slip*) or a localized mode (*coarse slip*), Lin and Argon (1994). During fine slip, the crystalline/amorphous interfaces remain intact while the coarse-slip mode initiates interface discontinuities and subsequent lamellae fragmentation (Fig. 1).

2.2. Amorphous phase

During crystallization, almost all entanglements and most of the branches of the polymer chains are expelled in the amorphous phase layers (e.g. Lin and Argon, 1994). Consequently, the amorphous phase of the semi-crystalline polymers consists of disordered molecules with high concentrations of entanglements and other defects. Above the glass transition temperature, the amorphous phase is in a rubber-like state with a pronounced viscoelastic behavior. Below the glass transition temperature, the mobility of the polymer segments is strongly reduced and the amorphous phase displays elasto—viscoplastic behavior. The amorphous phase of HDPE at room temperature is rubber-like viscoelastic. However, the experimental evidence suggests that for this polymer, the purely elastic strain is much smaller than the viscoelastic strain and can be neglected in a first approximation. In addition, as we consider only monotonous loadings, we cannot distinguish between viscoelasticity and viscoplasticity. Taking into account these considerations, in this work we apply a viscoplastic-like modeling of the amorphous phase.

Two main deformation modes have been identified for the amorphous layers, namely, interlamellar shear and interlamellar separation (e.g. Lin and Argon, 1994). In the context of incompressible deformation without cavitation assumed here, interlamellar separation is excluded as a deformation mode. We can therefore express the plastic velocity gradient resulting from interlamellar shear $\mathbf{L}_a^p$ in a given inclusion as:

$$\mathbf{L}_a^p = \dot{\gamma}_a(\mathbf{b}^{(a)} \otimes \mathbf{n}^{(I)}), \tag{5}$$

where $\dot{\gamma}_a$ is the amorphous phase shear rate, $\mathbf{b}^{(a)}$ is the direction of the interlamellar shear and $\mathbf{n}^{(I)}$ denotes the normal unit vector to the crystalline/amorphous interfaces in the inclusion (Fig. 2).

It is assumed that the direction of the interlamellar shear coincides with the projection $\mathbf{t}^{(a)}$ of the amorphous phase stress vector $(\mathbf{s}_a \cdot \mathbf{n}^{(I)})$ on the lamellae surfaces (Nikolov

et al., 2002). We can, therefore, write

$$\mathbf{b}^{(a)} = \frac{\mathbf{t}^{(a)}}{\|\mathbf{t}^{(a)}\|},$$

$$\mathbf{t}^{(a)} = \mathbf{s}_a \cdot \mathbf{n}^{(I)} - [(\mathbf{s}_a \cdot \mathbf{n}^{(I)}) \cdot \mathbf{n}^{(I)}]\mathbf{n}^{(I)},$$

$$\tau_a \equiv \frac{1}{2}\mathbf{s}_a : (\mathbf{b}^{(a)} \otimes \mathbf{n}^{(I)} + \mathbf{n}^{(I)} \otimes \mathbf{b}^{(a)}) = \mathbf{s}_a : \mathbf{R}^{(a)}(\mathbf{s}_a) = \|\mathbf{t}^{(a)}\|, \tag{6}$$

where $\mathbf{s}_a$ is the deviatoric part of the Cauchy stress in the amorphous phase and τ_a is the effective shear stress. It is noted that τ_a is a positive quantity by construction and the amorphous phase (symmetric) Schmid tensor $\mathbf{R}^{(a)}$ depends on the applied stress $\mathbf{s}_a$ through $\mathbf{b}^{(a)}$.

The relation between the amorphous phase shear rate $\dot{\gamma}_a$ and the effective shear stress is given by (van Dommelen et al., 2003):

$$\dot{\gamma}_a = \dot{\gamma}_0 \left(\frac{\tau_a}{g_a}\right)^{n_a} \tag{7}$$

with g_a being the shear strength of the amorphous layers and n_a the rate exponent (inverse of rate sensitivity) of the amorphous phase. The reference shear rate $\dot{\gamma}_0$ is taken to be the same for both the amorphous and crystalline phase.

To complete the constitutive modeling, we need to introduce the amorphous phase hardening due to the strain-induced molecular alignment as well as its locking caused by (i) the finite extensibility of the polymer strands and (ii) the onset of coarse slip that makes the interlamellar shear kinematically unfavorable.

The hardening of the amorphous phase is usually modeled as a back stress (Lee et al., 1993a; van Dommelen et al., 2003 expressed with the rubber elasticity model of Arruda and Boyce (1993) as:

$$\mathbf{h}_a = \frac{\mu_R}{3} \sqrt{\frac{3N}{I_1}} \mathscr{L}^{-1}\left(\sqrt{\frac{I_1}{3N}}\right)\left(\mathbf{b}_a - \frac{1}{3}I_1 \mathbf{1}\right), \tag{8}$$

where μ_R is the rubbery shear modulus; N is the number of rigid links (with length l) constituting the sub-chains between entanglements; $\mathbf{b}_a$ is the left Cauchy–Green strain tensor of the amorphous phase; I_1 is the trace of $\mathbf{b}_a$; $\mathscr{L}^{-1}(x)$ is the inverse of the Langevin function $\mathscr{L}(x) = \coth(x) - 1/x$.

Here we apply a different approach. Because interlamellar separation is excluded in our model, the back stress given by Eq. (8) will result only from amorphous phase shear with shear stress h_a and will be aligned with the effective shear stress τ_a but with an opposite direction. On the other hand, it is always possible to choose the reference shear rate in Eq. (7) such that $\dot{\gamma}_a = \dot{\gamma}_0$. Then, from Eq. (7) it follows that:

$$\left(\frac{\tau_a - h_a}{g_a}\right)_{\dot{\gamma}_a = \dot{\gamma}_0} = \left(\frac{\tau_a}{g_a + h_a}\right). \tag{9}$$

The above considerations indicate that instead of using the back stress $\mathbf{h}_a$ given by Eq. (8), we can alternatively use a "crystallographic extension" of the Arruda–Boyce model where the back stress is introduced as a nonlinear strain hardening, h_a, of the shear resistance, g_a, of the "slip system" associated with the interlamellar shear. A similar "crystallographic extension" of an "isotropic" material model at the level of the slip systems in a single

crystal was proposed by Kok et al. (2002) in the context of a crystal plasticity-based FE analysis.

The rubber-like hardening h_a can be computed analytically by solving the constitutive equation (8) for simple shear deformation. In a local Cartesian basis $(\mathbf{e}_1, \mathbf{e}_2, \mathbf{e}_3)$, the left Cauchy–Green strain resulting from shear strain γ_a on the slip system $\mathbf{e}_1 \otimes \mathbf{e}_2$ is given by (e.g. Doghri, 2000):

$$\mathbf{b}_a = \begin{pmatrix} 1 + \gamma_a^2 & \gamma_a & 0 \\ \gamma_a & 1 & 0 \\ 0 & 0 & 1 \end{pmatrix} \tag{10}$$

with the principal invariant $I_1 = 3 + \gamma_a^2$.

The Padé approximation of the inverse Langevin function derived by Cohen (1991) reads $\mathcal{L}^{-1}(x) = x(3 - x^2)/(1 - x^2)$. Then, from Eqs. (8) and (10) we obtain the shear back force, or, equivalently, the hardening of the slip resistance of the amorphous phase as:

$$h_a = \frac{\mu_R}{3} \frac{(9N - 3 - \gamma_a^2)}{(3N - 3 - \gamma_a^2)} \gamma_a. \tag{11}$$

With the above considerations in mind, the constitutive equations for the amorphous phase can be summarized as follows:

$$\begin{aligned}
\mathbf{L}_a^p &= \mathbf{D}_a^p + \mathbf{W}_a^p, \\
\mathbf{D}_a^p &= \dot{\gamma}_a \mathbf{R}^{(a)}, \\
\mathbf{W}_a^p &= \dot{\gamma}_a \mathbf{A}^{(a)}, \\
\dot{\gamma}_a &= \dot{\gamma}_0 \left(\frac{\tau_a}{g_a + h_a} \right)^{n_a}, \\
\tau_a &= \| \mathbf{s}_a \cdot \mathbf{n}^{(I)} - [(\mathbf{s}_a \cdot \mathbf{n}^{(I)}) \cdot \mathbf{n}^{(I)}] \mathbf{n}^{(I)} \|, \\
h_a &= \frac{\mu_R}{3} \frac{(9N - 3 - \gamma_a^2)}{(3N - 3 - \gamma_a^2)} \gamma_a,
\end{aligned} \tag{12}$$

where plastic deformation without rigid rotation is considered.

2.3. Composite inclusion

The undeformed composite inclusion is depicted in Fig. 2b. The crystalline phase content χ_c in each inclusion is taken to be equal to the overall crystallinity. Similarly to the decomposition suggested by Lee for elastic–plastic behavior (Lee, 1969), the deformation gradient $\mathbf{F}_I$ in a given inclusion can be separated into plastic deformation that preserves the orientation $\mathbf{F}_I^p$ and a rigid rotation $\mathbf{F}_I^*$:

$$\mathbf{F}_I = \mathbf{F}_I^* \cdot \mathbf{F}_I^p = \mathbf{R}_I \cdot \mathbf{F}_I^p, \tag{13}$$

where $\mathbf{R}_I \equiv \mathbf{F}_I^*$ is the rotation matrix of the inclusion. It can be obtained from the right polar decomposition $\mathbf{F}_I = \mathbf{R}_I \cdot \mathbf{U}_I$.

The inclusion's velocity gradient $\mathbf{L}_I$ is related to the corresponding deformation gradient $\mathbf{F}_I$ via $\mathbf{L}_I = \dot{\mathbf{F}}_I \cdot \mathbf{F}_I^{-1}$. By introducing Eq. (13) into the latter definition, $\mathbf{L}_I$ is decomposed

into the rate of deformation $\mathbf{D}_I$ and the spin $\mathbf{W}_I$ of the inclusion:

$$\mathbf{L}_I = \mathbf{D}_I + \mathbf{W}_I. \tag{14}$$

The components of $\mathbf{D}_I$ and $\mathbf{W}_I$ involving plastic deformation without rigid rotation are assumed to be the volume averages of the plastic rate of deformation and spin tensors in the phases (Eqs. (2b), (2c), (12b) and (12c)):

$$\mathbf{D}_I^p = \chi_c \mathbf{D}_c^p + (1 - \chi_c)\mathbf{D}_a^p,$$
$$\mathbf{W}_I^p = \chi_c \mathbf{W}_c^p + (1 - \chi_c)\mathbf{W}_a^p. \tag{15}$$

With Eqs. (13)–(15), $\mathbf{D}_I$ and $\mathbf{W}_I$ are expressed as follows:

$$\mathbf{D}_I = \mathbf{R}_I \cdot \mathbf{D}_I^p \cdot \mathbf{R}_I^T,$$
$$\mathbf{W}_I = \dot{\mathbf{R}}_I \cdot \mathbf{R}_I^T + \mathbf{R}_I \cdot \mathbf{W}_I^p \cdot \mathbf{R}_I^T. \tag{16}$$

Continuity of traction on the interface requires that

$$\mathbf{s}_I \cdot \mathbf{n}^{(I)} = \mathbf{s}_c \cdot \mathbf{n}^{(I)} = \mathbf{s}_a \cdot \mathbf{n}^{(I)}. \tag{17}$$

With regard to the stresses in the crystalline and amorphous phases, it is useful to recall some experimental evidence, namely, that prior to yield, the strain is entirely accommodated by the amorphous phase and that rigid rotation of lamellae stacks takes place at larger strains (Lin and Argon, 1994). This indicates that the interactions between the lamellae stacks are weak and the variations of the local stress in semi-crystalline polymers must be much smaller compared to the stress variations observed in metals and alloys, for example. On the other hand, previous models (Lee et al., 1993a) were successful in the simulation of semi-crystalline polymers using a Sachs-type assumption for uniform stress. For the sake of simplicity and in order to facilitate the numerical implementation, here we assume that the deviatoric stress within the inclusion, $\mathbf{s}_I$, is uniform and equal for both phases, which corresponds to a Sachs-type assumption for the lamellar inclusion:

$$\mathbf{s}_I = \mathbf{s}_c = \mathbf{s}_a. \tag{18}$$

The above approximation ensures that equilibrium within the inclusion and Eq. (17) are trivially satisfied. In addition, as shown in Nikolov et al. (2002), this assumption is not too restrictive. Taking into account Eq. (12e) and the incompressibility in both phases, it follows that only two scalar identities embedded in Eq. (18) are additionally imposed on the inclusion beyond the traction equilibrium conditions expressed by Eq. (17) namely:

$$(s_I)_{11} = (s_c)_{11} \quad \text{or} \quad (s_I)_{22} = (s_c)_{22}, \quad (s_I)_{12} = (s_c)_{12}, \tag{19}$$

where the components are written in a local Cartesian basis with the third direction $\mathbf{e}_3 \equiv \mathbf{n}^{(I)}$.

   The compatibility conditions at the inclusion level are not explicitly enforced in our model for two reasons. Firstly, they are not needed in the single-crystal-like constitutive modeling of the lamellae stacks where the amorphous phase deformation is formally introduced as an additional degree of freedom for microscopic shear. Thus, if the number of the available slip systems in the polymer crystals is P, the composite inclusion has $P + 1$ slip systems where the (variable) direction of the amorphous phase shear is given by Eqs. (6a) and (6b). At any rate, the number of independent slip systems in the inclusion is not an issue here because even if a single inclusion cannot accommodate an imposed general deformation, our self-consistent approach allows us to obtain a unique solution for

the macroscopic properties of the aggregate. Secondly, the formulation of realistic compatibility conditions is extremely difficult in our case because in general, due to the lamellae kinking and disruption, the crystalline/amorphous interfaces do not remain flat and intact during deformation, as observed, for example, in tensile experiments (see Fig. 1).

Finally, we consider the influence of coarse slip and lamellae kinking on the kinematics of the lamellae stacks. As illustrated in Fig. 1, the onset of coarse slip in the crystalline lamellae can lock the amorphous phase shear *well before* the amorphous phase molecules have reached their limit stretch, Nl, with N and l being the number and the length of the rigid segments building the chains, respectively. This suggests that the interplay between the crystalline and amorphous phase during deformation of semi-crystalline polymers is much more complicated than in bi-crystals where the deformation in one phase does not directly influence the kinematics of the other and the integrity of the interfaces is preserved at all strains. In order to account for the influence of the crystalline phase deformation on the amorphous phase hardening during coarse slip, we propose a simple modification of the hardening law, Eq. (11), where the amorphous phase strain, γ_a, is replaced by the accumulated viscoplastic strain in the inclusion:

$$h_a = \frac{\mu_R}{3} \frac{(9N - 3 - \Gamma^2)}{(3N - 3 - \Gamma^2)} \Gamma \tag{20}$$

with

$$\Gamma(t) = \int_0^t \left(\chi_c \sum_\alpha |\dot{\gamma}_\alpha| + (1 - \chi_c)|\dot{\gamma}_a| \right) d\tau \tag{21}$$

being the accumulated viscoplastic strain in the inclusion.

In cases where coarse slip does not take place, for example at temperatures above the α-transition where the chain mobility in the crystals abruptly increases, the hardening law given by Eq. (11) should be used.

3. Macroscopic properties and evolution of the microstructure

3.1. Self-consistent interaction law

In order to identify the effective properties of the aggregate, it is necessary to formulate an interaction law that relates the mechanical behavior of each composite inclusion to the macroscopically imposed boundary conditions, so that the following self-consistent conditions are satisfied:

$$\bar{\mathbf{s}} = \langle \mathbf{s}_I \rangle, \quad \overline{\mathbf{D}} = \langle \mathbf{D}_I \rangle, \quad \overline{\mathbf{W}} = \langle \mathbf{W}_I \rangle, \tag{22}$$

where $\bar{\mathbf{s}}$, $\overline{\mathbf{D}}$ and $\overline{\mathbf{W}}$ are the overall deviatoric stress, rate of deformation, and spin tensors, respectively. Throughout the text, the brackets $\langle \cdot \rangle$ denote volume averages over all inclusions in the aggregate.

The 1-site self consistent approach considers each (composite) inclusion as embedded in a Homogeneous Equivalent Medium (HEM) representing the surrounding material (Molinari et al., 1987). Both equilibrium and compatibility at the inclusion's boundaries are enforced in a strong sense when using the HEM approach. Unlike either the Taylor assumption for uniform strain rate or the Sachs model imposing uniform stress throughout

the aggregate, the self-consistent method predicts both stress and strain rate heterogeneity depending on the local properties, such that the conditions given by Eq. (22) are met. On the other hand, the classical self consistent approach used here is different from the hybrid self-consistent-like interaction laws developed by Lee et al. (1993a) and van Dommelen et al. (2003) where the compatibility and equilibrium of a given inclusion with the rest of the material is defined not with respect to the inclusion's outer boundaries but to its crystalline/amorphous interface.

In this work, we use the tangent viscoplastic formulation proposed by Lebensohn and Tomé (1993). From the Sachs-type assumption, Eq. (18), it follows that the homogenized compliance of a given inclusion, $\mathbf{M}_I$, is the volume average of the viscoplastic compliances of the crystalline and amorphous phases. Hence, the rate of deformation, $\mathbf{D}_I$, can be expressed as:

$$\mathbf{D}_I = [\chi_c \mathbf{M}_c + (1 - \chi_c)\mathbf{M}_a] : \mathbf{s}_I = \mathbf{M}_I : \mathbf{s}_I,$$

$$\mathbf{M}_c = \sum_\alpha \left(\frac{\dot{\gamma}_0}{g_\alpha} \left| \frac{\tau_\alpha}{g_\alpha} \right|^{n_c - 1} \mathscr{R}^{(\alpha)} \otimes \mathscr{R}^{(\alpha)} \right),$$

$$\mathbf{M}_a = \frac{\dot{\gamma}_0}{g_a + h_a} \left| \frac{\tau_a}{g_a + h_a} \right|^{n_a - 1} \mathscr{R}^{(a)} \otimes \mathscr{R}^{(a)}, \tag{23}$$

where $\mathscr{R}^{(\alpha)} = \mathbf{R}_I \cdot \mathbf{R}^{(\alpha)} \cdot \mathbf{R}_I^T$ and $\mathscr{R}^{(a)} = \mathbf{R}_I \cdot \mathbf{R}^{(a)} \cdot \mathbf{R}_I^T$ are the symmetric Schmid tensors of the crystalline and amorphous phases, respectively, rotated from the intermediate to the current configuration. The compliances of the crystalline and amorphous phases are denoted by $\mathbf{M}_c$ and $\mathbf{M}_a$, respectively.

The deviation between the rate of deformation, $\mathbf{D}_I$, in a given inclusion and the imposed macroscopic rate, $\overline{\mathbf{D}}$, is related to the inclusion's deviatoric stress, $\mathbf{s}_I$, and the overall stress, $\overline{\mathbf{s}}$, via the interaction law (Lebensohn and Tomé, 1993):

$$(\mathbf{D}_I - \overline{\mathbf{D}}) = -\tilde{\mathbf{M}}_I : (\mathbf{s}_I - \overline{\mathbf{s}}), \tag{24}$$

where

$$\tilde{\mathbf{M}}_I = n(\mathbf{I} - \mathbf{S}_I)^{-1} : \mathbf{S}_I : \overline{\mathbf{M}}, \tag{25}$$

is the so-called interaction tensor; n is the rate exponent of the inclusion. For simplicity, we assume that the rate exponents of the phases are equal for all inclusions so that $n = n_c = n_a$; $\mathbf{S}_I$ is the viscoplastic Eshelby tensor depending on the inclusion's shape and the overall secant compliance, $\overline{\mathbf{M}}$, given by

$$\overline{\mathbf{M}} = \langle \mathbf{M}_I : \mathbf{B}_I \rangle, \tag{26}$$

where $\mathbf{B}_I$ is the localization tensor defined as

$$\mathbf{B}_I = (\mathbf{M}_I + \tilde{\mathbf{M}}_I)^{-1} : (\overline{\mathbf{M}} + \tilde{\mathbf{M}}_I). \tag{27}$$

Here it is assumed that all the inclusions have the same initial morphology and that their shape and orientation are updated according to the macroscopic deformation gradient (see Section 3.2), so that their morphology remains unique. In general, when the shape and the orientation differ from one inclusion to another, a modified self-consistent equation must be introduced (Walpole, 1969; Lebensohn et al., 1996).

3.2. Texture and morphology update

We consider a generic time interval $[t, t + \Delta t]$. The velocity gradient $\mathbf{L}_I$ in each inclusion at a time t is known and is assumed to remain constant during the time increment Δt.

The rate of change of the rotation matrix $\mathbf{R}_I$ that governs the texture evolution is obtained from Eq. (16b) as:

$$\dot{\mathbf{R}}_I = (\mathbf{W}_I - \mathbf{W}_I^p) \cdot \mathbf{R}_I \tag{28}$$

The updated rotation matrix is found from:

$$\mathbf{R}_I^{t+\Delta t} = \mathbf{R}_I^t + (\mathbf{W}_I - \mathbf{W}_I^p) \cdot \mathbf{R}_I^t \Delta t \tag{29}$$

The deformation gradient in a given inclusion $\mathbf{F}_I$ is updated using the macroscopic velocity gradient $\overline{\mathbf{L}} = \overline{\mathbf{D}} + \overline{\mathbf{W}}$ and the relation $\dot{\mathbf{F}}_I = \overline{\mathbf{L}} \cdot \mathbf{F}_I^t$:

$$\mathbf{F}_I^{t+\Delta t} = \mathbf{F}_I^t + \dot{\mathbf{F}}_I \Delta t = (\mathbf{I} + \overline{\mathbf{L}} \Delta t) \cdot \mathbf{F}_I^t. \tag{30}$$

The deformation gradient computed with the help of Eq. (30) is then used to update the shape of the inclusions as follows. In the reference configuration at $t = 0$, all inclusions are assumed to have spherical shape. Then, the points at the boundary of a given inclusion have position vectors $\mathbf{X}$ in the reference configuration defined by $\mathbf{X} \cdot \mathbf{X} = 1$. In the deformed configuration, the position vectors become $\mathbf{x} = \mathbf{F}_I \cdot \mathbf{X}$. The corresponding locus is found from:

$$[(\mathbf{F}_I \cdot \mathbf{F}_I^T)^{-1} \cdot \mathbf{x}] \cdot \mathbf{x} = 1. \tag{31}$$

Eq. (31) is that of a general ellipsoid. The eigenvectors and the square root of the eigenvalues of $\mathbf{F}_I \cdot \mathbf{F}_I^T$ define the direction and the length of the ellipsoid axes, respectively.

4. Applications and results

4.1. Model parameters

The micromechanical model has been implemented in the self-consistent code VPSC6 (Lebensohn and Tomé, 2003). HDPE at room temperature is chosen as a model material. The undeformed polymer is represented as an aggregate of 500 randomly oriented composite inclusions with an initially spherical shape. The tilt angle between the lamellae normals and the chain direction in the crystals (Fig. 2) is chosen as $(\mathbf{n}^{(1)}, \mathbf{c}) = 34.4°$. This value corresponds to the $\{2\,0\,1\}$ orientation of the interfaces, according to experimental (Bassett and Hodge, 1981) and theoretical (Gautam et al., 2000) results for polyethylene. The crystallinity content in the inclusions is fixed at $\chi_c = 0.7$, which is a typical value for HDPE. The rate exponents and the reference shear rate are taken to be $n_a = n_c = 9$ and $\dot{\gamma}_0 = 10^{-3}\,\mathrm{s}^{-1}$, respectively (Lee et al., 1993a).

The orthorhombic unit cell of a polyethylene crystal has dimensions $a = 7.4\,\text{Å}; b = 4.93\,\text{Å}; c = 2.54\,\text{Å}$ with c being the lattice parameter along the polymer chains. The associated eight slip systems (of which only four are independent) and the corresponding shear resistances used in the present work are listed in Table 1.

The initial shear resistance of the additional "slip system" due to amorphous phase shear (which, applied to HDPE, increases the number of independent slip systems in a single composite inclusion to five) is chosen as $g_a = 3.4\,\mathrm{MPa}$. According to the

Table 1
Slip systems and resistances of HDPE crystals used in this work

	Slip system	g_α (MPa)
Chain slip	(1 0 0)[0 0 1]	7.2[a]
	(0 1 0)[0 0 1]	15.6[a]
	{1 1 0}[0 0 1]	15.6 (>13[a])
Transverse slip	(1 0 0)[0 1 0]	12.2[a]
	(0 1 0)[1 0 0]	18[b]
	{1 1 0}⟨1 $\bar{1}$ 0⟩	15.9[b]

$(\cdot)$[a]—experimentally measured resistances from Bartczak et al. (1992b).
$(\cdot)$[b]—resistances with ratio $g_\alpha/g_{(1\,0\,0)[0\,0\,1]}$ taken from Lee et al. (1993a).

observations, at room temperature the interlamellar shear is the most easily activated deformation mode for HDPE (Lin and Argon, 1994). Coarse slip is taken into account with the numerical implementation of the hardening law given by Eqs. (20) and (21). The amorphous phase rubbery modulus and the number of rigid links of the sub-chains have been identified as $\mu_R = 12$ MPa and $N = 8$, respectively. For comparison, Lee et al. (1993b) used $\mu_R = 0.8$ MPa and $N = 12$. The higher value of μ_R in our model suggests that the amorphous phase layers may be stiffer than a conventional rubber because (i) they contain more entanglements and branches than the polymer melt before crystallization and (ii) for HDPE, the amorphous layers thickness is only of the order of 10 nm so that size effects could be the cause for additional stiffening.

The above values for the model parameters have been chosen to adjust the experimental stress–strain curve in uniaxial compression and then used without further change for prediction of uniaxial tension and simple shear.

4.2. Uniaxial compression

The first application is uniaxial compression of a HDPE sample at a constant strain rate of 10^{-3} s^{-1}. In Fig. 3, the predicted equivalent stress ($\overline{\sigma}_{eq} = \sqrt{\frac{3}{2}\overline{s}_{ij}\overline{s}_{ij}}$) versus strain ($\overline{\varepsilon}_{eq} = \int_0^t \overline{D}_{eq}\,d\tau$) curve is compared with the measured true stress–strain response obtained by Bartczak et al. (1992a) and the predictions of Lee et al. (1993b). The macroscopic true strain rate is defined as the equivalent strain rate, $\overline{D}_{eq} = \sqrt{\frac{2}{3}\overline{D}_{ij}\overline{D}_{ij}}$.

For equivalent strains $\overline{\varepsilon}_{eq} < 1$, the predictions of the present model and the results of Lee et al. (1993b) are very close to each other and agree well with the experiment. At larger strains, however, the present model predicts a slightly more realistic stress–strain response. According to Fig. 12, the reason for that is *not* the rubbery hardening of the amorphous phase but the morphological evolution of the composite inclusions.

Fig. 4 shows in the left diagram the normalized strain rates (hereafter referred to as relative activity) of the principal deformation modes in the phases versus $\overline{\varepsilon}_{eq}$. We distinguish between chain slip, transverse slip and interlamellar shear (which in our model represents the total amorphous phase deformation). It is emphasized that at smaller strains, chain and transverse slip operate solely in the crystalline phase. At very large strains and strong evolution of the shape of the inclusions, however, they should be
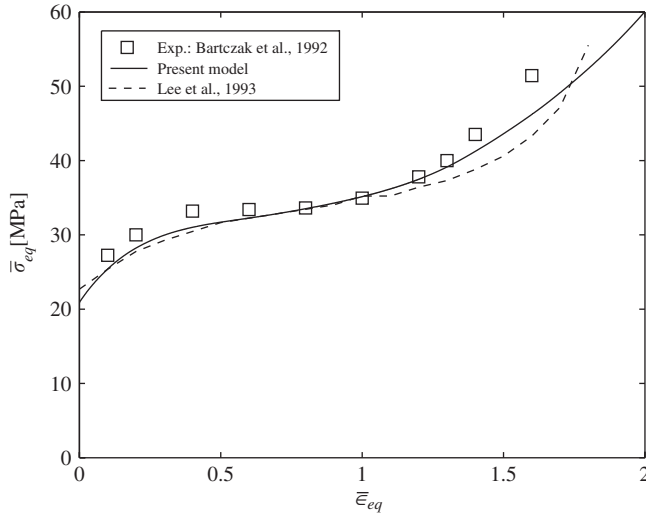
Fig. 3. Predicted and measured stress–strain curves for HDPE in uniaxial compression.
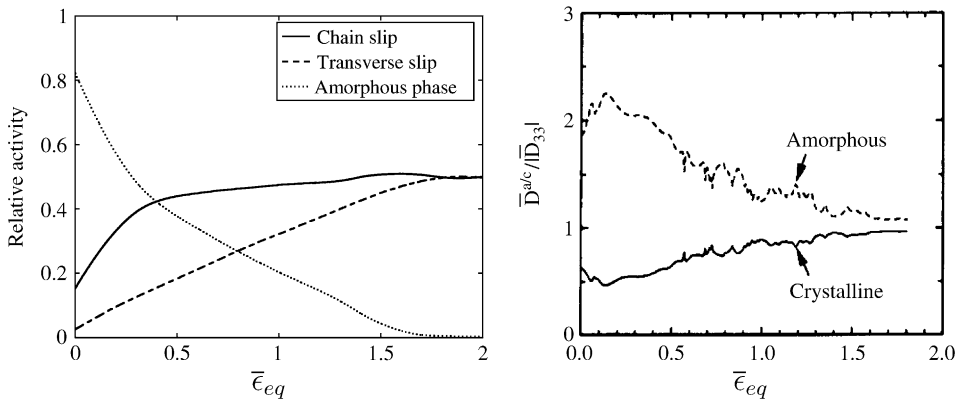
Fig. 4. Relative activity of the principal deformation modes in the phases vs. $\bar{\varepsilon}_{eq}$ in uniaxial compression. Left: present model; Right: according to Lee et al. (1993b).

interpreted as chain and transverse shear between composite micro-fibrils formed after the lamellae disruption. According to Fig. 4, left, at small strains the amorphous phase deforms much faster than the crystals, but its activity rapidly decreases with increasing $\bar{\varepsilon}_{eq}$ and at $\bar{\varepsilon}_{eq} > 1.7$ it is practically locked. At $\bar{\varepsilon}_{eq} > 0.4$, chain slip is the dominant deformation mode up to very large strains where the steadily evolving transverse slip becomes equally important. The corresponding results obtained by Lee et al. (1993b) are shown in Fig. 4, right. It is seen that the amorphous phase strain rate is superior to the strain rate in the crystals at all deformation levels and saturates with increasing $\bar{\varepsilon}_{eq}$, but at a much slower pace compared to our prediction, and never locks.

Next, we analyze the texture evolution. In the present work, the predicted pole figures are obtained with a TSL OIM Analysis software. Fig. 5 shows the predicted equal-area-projection
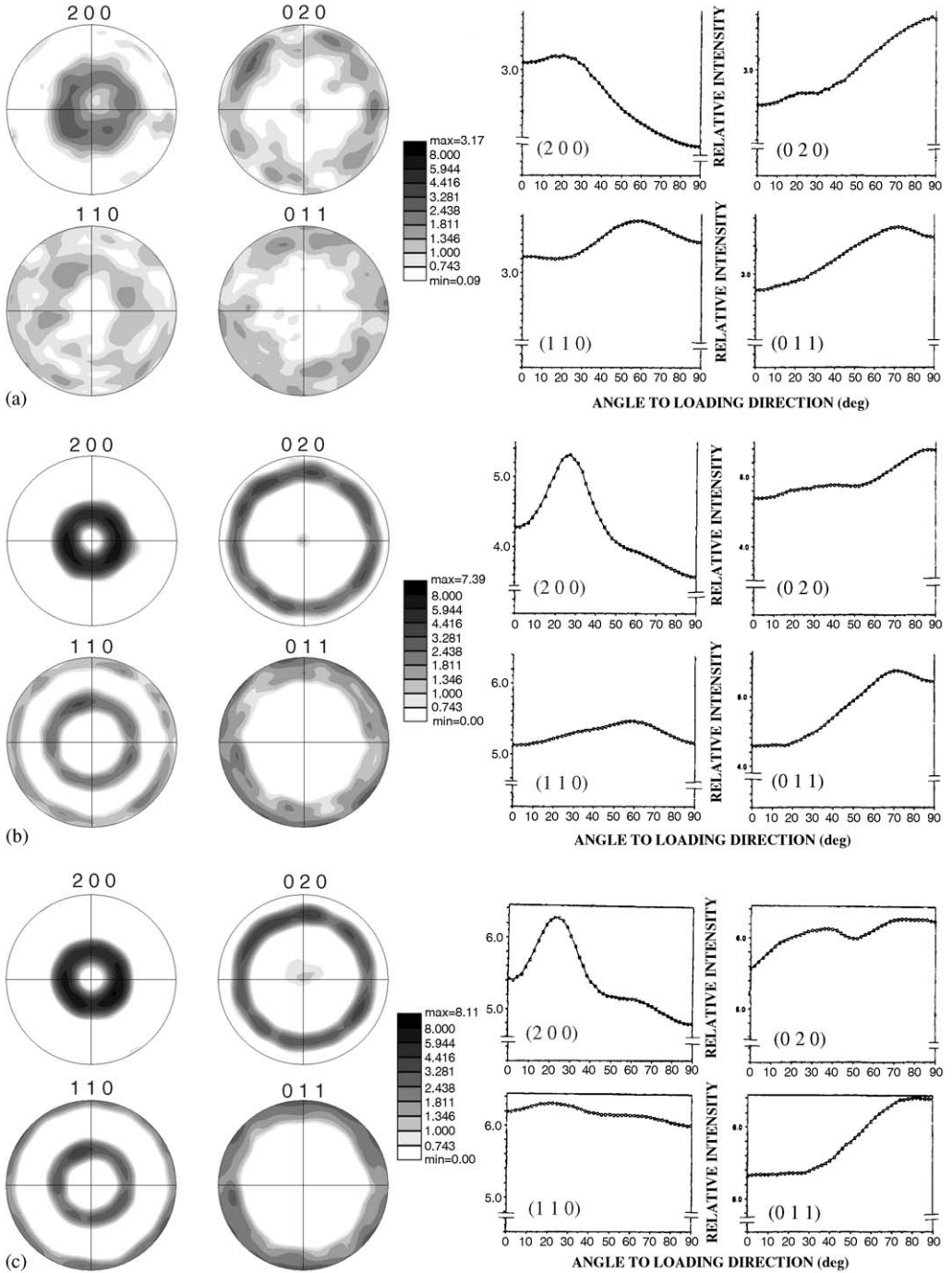
Fig. 5. Left: predicted pole figures in uniaxial compression at equivalent strains, (a) $\bar{\varepsilon}_{eq} = 0.35$; (b) $\bar{\varepsilon}_{eq} = 1.29$; (c) $\bar{\varepsilon}_{eq} = 1.86$. The loading direction is normal to the equator plane of the figure. Right: corresponding experimental intensities obtained by Bartczak et al. (1992a).

pole figures, compared to the experimental intensities measured by Bartczak et al. (1992a). The $(2\,0\,0)$, $(0\,2\,0)$ and $(0\,0\,2)$ planes correspond to the **a**, **b** and **c** crystallographic axes, respectively. In accordance with the experiments, the predicted pole figures display axial symmetry with respect to the compressive direction.

At plastic strain $\bar{\varepsilon}_{eq} = 0.35$, the chain $(1\,0\,0)[0\,0\,1]$ slip is the most active deformation mode in the crystals. Consequently, the **a** and **b** crystal axes migrate towards and away from the compressive direction, respectively. Experimentally, the maximum intensity for the $(2\,0\,0)$ planes is located at an angle of about $25°$ to the loading direction (LD). For the $(0\,2\,0)$, $(1\,1\,0)$ and $(0\,1\,1)$ planes, the corresponding maximum intensities are located at about $85°$, $60°$ and $70°$, respectively; the $(1\,1\,0)$ planes show a very weak texturing.

At a strain $\bar{\varepsilon}_{eq} = 1.29$, intense lamellae kinking and rearrangement has already taken place (Bartczak et al., 1992a) and both chain and transverse slip are active. This results in the development of a sharp maximum in the intensity of the $(2\,0\,0)$ planes' distribution. The location of the maximum, however, is not affected. The **b** axes are mostly arranged at about $80°$ to LD. The $(0\,1\,1)$ planes are depleted in the center of the pole figure and gradually arrange circumferentially towards the radial direction. Their maximum intensity remains at about the same angle to LD. The $(1\,1\,0)$ planes have developed a weak texture with maximum intensity located at about $55°$ to LD.

At a strain $\bar{\varepsilon}_{eq} = 1.86$, the predicted texture does not change qualitatively with respect to that obtained for $\bar{\varepsilon}_{eq} = 1.29$. Besides further sharpening in terms of intensities, it is noted that the maxima of the $(0\,2\,0)$ and $(1\,1\,0)$ planes have moved towards the LD and are located at $75°$ and $35°$, respectively. The $(0\,1\,1)$ planes reach the direction of $90°$ with respect to the compressive axis.

From Fig. 5, it is seen that the model predictions for the texture evolution during uniaxial compression compare favorably with the experiment, although the chosen form of presentation of the experimental results in Bartczak et al. (1992a) makes the direct quantitative comparison somewhat difficult.

4.3. Uniaxial tension

Next, we simulate an uniaxial tensile experiment at a constant true strain rate $\overline{D}_{eq} = 10^{-3}\,\text{s}^{-1}$. In uniaxial tension, HDPE displays necking instability and cavitation immediately after the yield point, which poses difficulties in obtaining the true stress–strain curves. This problem was solved by G'Sell and Jonas (1979) who developed a special device maintaining a constant strain rate in the center of the neck. In Fig. 6, the simulated stress–strain behavior is compared to experimental data from G'Sell and Jonas (1979) and Hiss et al. (1999) obtained with this technique, as well as to the results reported in Lee et al. (1993b).

It is seen that both models give similar predictions for strains $\bar{\varepsilon}_{eq} < 1$. For $\bar{\varepsilon}_{eq} < 0.5$, our model slightly overestimates the stress triaxiality, which results in a higher-than-measured equivalent stress. For strains $\bar{\varepsilon}_{eq} > 1$, the present model agrees much better with the experiment than the results of Lee et al. (1993b). These authors argued that strain-induced cavitation results in higher effective stress than that measured experimentally. Dahoun (1992), however, measured the decrease in density ρ during tension of HDPE and showed that for $\bar{\varepsilon}_{eq} \approx 1.5$, $\rho/\rho_0 \approx 0.9$ with ρ_0 the initial density. Therefore, cavitation cannot explain the significant deviation of the results of Lee et al. (1993b) from the experiment.
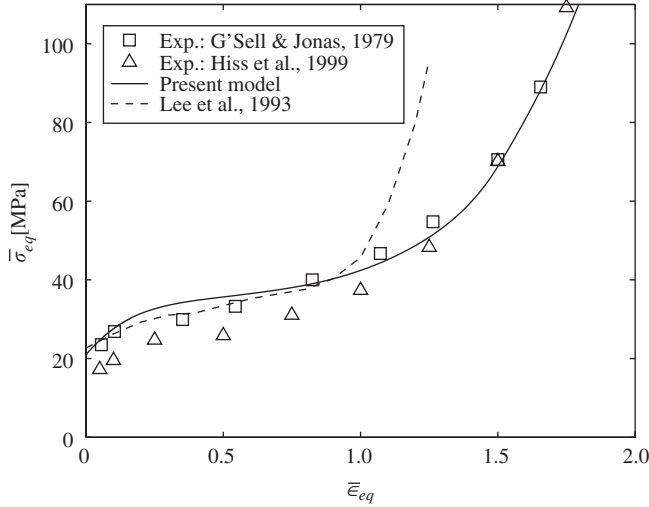
Fig. 6. Predicted and measured stress–strain curves for HDPE in uniaxial tension.
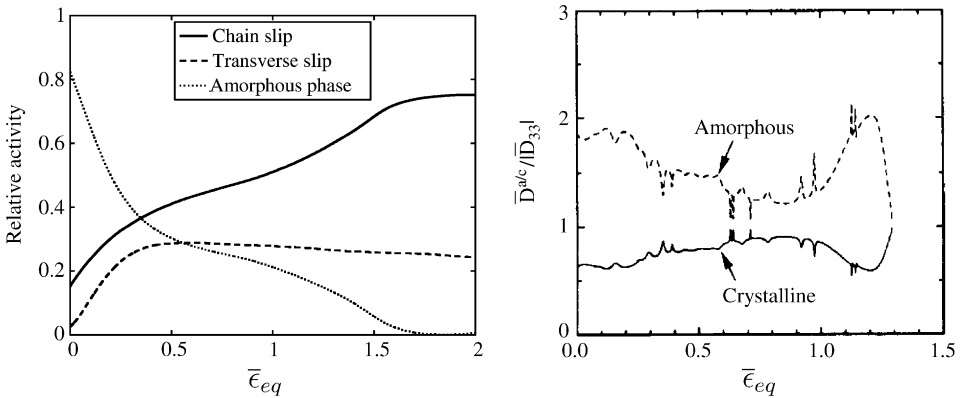
Fig. 7. Relative activity of the principal deformation modes in the phases vs. $\bar{\varepsilon}_{eq}$ in uniaxial tension. Left: present model; Right: according to Lee et al. (1993b).

Although with less influence than in uniaxial compression, the morphology evolution (Fig. 12) explains in part the ability of our model to match the experiment at very large strains. While the actual processes involved into the lamellar-to-fibrillar transition shown in Fig. 1 are much more complex than our modeling, the obtained results suggest that in a first approximation, this morphology change can be accounted for reasonably well through the change of shape of the inclusions and the crystallographic texture evolution within the inclusions. The choice of averaging scheme and the constitutive model for the composite inclusions are the other important factors that determine the predicted stress–strain response.

The relative activity of the crystalline and amorphous phases in function of $\bar{\varepsilon}_{eq}$ during tension is shown in Fig. 7, left. The amorphous phase strain rate follows a pattern very

similar to that in uniaxial compression and locks at $\bar{\varepsilon}_{eq} > 1.7$. With increasing strain, chain slip becomes the dominant deformation mode and its strain rate increases up to strains $\bar{\varepsilon}_{eq} \approx 1.7$, thus contributing to the development of a very strong **c** texture component along the tensile direction. Transverse slip is most active at a strain $\bar{\varepsilon}_{eq} \approx 0.4$, but unlike in compression, its strain rate steadily decreases for $\bar{\varepsilon}_{eq} > 0.4$ in favor of the chain slip. The corresponding graphics obtained by Lee et al. (1993b) is depicted in Fig. 7, right. Again, it is seen that the amorphous phase behavior predicted by the two models is very different, especially at equivalent strains $\bar{\varepsilon}_{eq} > 1$ where, according to Lee et al. (1993b), the amorphous phase strain rate shows a steep increase and reaches a maximum at $\bar{\varepsilon}_{eq} = 1.2$ before locking.

The predicted and experimental pole figures for uniaxial tension are given in Fig. 8. The pole figures are obtained with harmonic series expansion for the intensity functions and plotted in stereographic projection. The experimental data from Li et al. (2001) represent the texture of a sample of HDPE after relaxation.[1] It is noted that in Fig. 8c, the (0 1 0) component aligned with the tensile direction has been found to be stronger during deformation.

At true strain $\bar{\varepsilon}_{eq} = 0.8$ (Fig. 8a), the predicted texture evolution is relatively weak and results from both chain and transverse slip. Most of the **c** axes are oriented at about 25° to the tensile direction, a smaller fraction is oriented in the radial direction. The **a** axes form an angle of about 65° with the LD, the **b** axes just start to form a weak component oriented at 25° away from the LD.

At true strain $\bar{\varepsilon}_{eq} = 2.1$, a very strong **c** fiber component develops along the tensile direction. The fraction of the radially oriented **c** axes remains unchanged, and a small fraction of crystals has **c** axes oriented at about 45° to the LD. Most of the **a** and **b** axes have migrated towards the radial direction, but our model also predicts a relatively strong (0 1 0) component oriented at about 25° to the LD and a very weak component oriented along the tensile direction.

Experimentally, the preferred orientations in HDPE at large strains have been found to be (Li et al., 2001): (i) a strong (0 0 1) component aligned with the tensile axis; (ii) a weaker (0 1 1) component aligned close to the tensile axis; (iii) a weaker (0 1 0) component aligned with the tensile axis. From Fig. 8b, it is seen that our model correctly predicts the existence of all three components, i.e., a strong **c** fiber; weaker (0 1 1) and (0 1 0) components more or less aligned with the tensile axis. In contrast to the experiment, we obtain a (0 1 0) component oriented at 25° instead of a perfect alignment with the tensile axis. The predicted average angle of the (0 1 1) planes is also somewhat wider than the experimentally measured one. We believe that these minor discrepancies are due to the fact that the lamellae breakage, which allows the lamellae pieces to rotate more freely at large tensile strains, is not explicitly incorporated in our model. It is noted, however, that the model gives considerably better predictions in tension compared to those reported in Lee et al. (1993a, b), where the **c** component develops much faster than observed and the (0 1 1) and (0 1 0) components along or close to the tensile direction are not predicted at all.

---

[1]Li et al. (2001) also measured the in-situ texture evolution during deformation, but we could not use these data because the HDPE sample displayed a strong texture in the undeformed state, which remained stable up to very high strains.
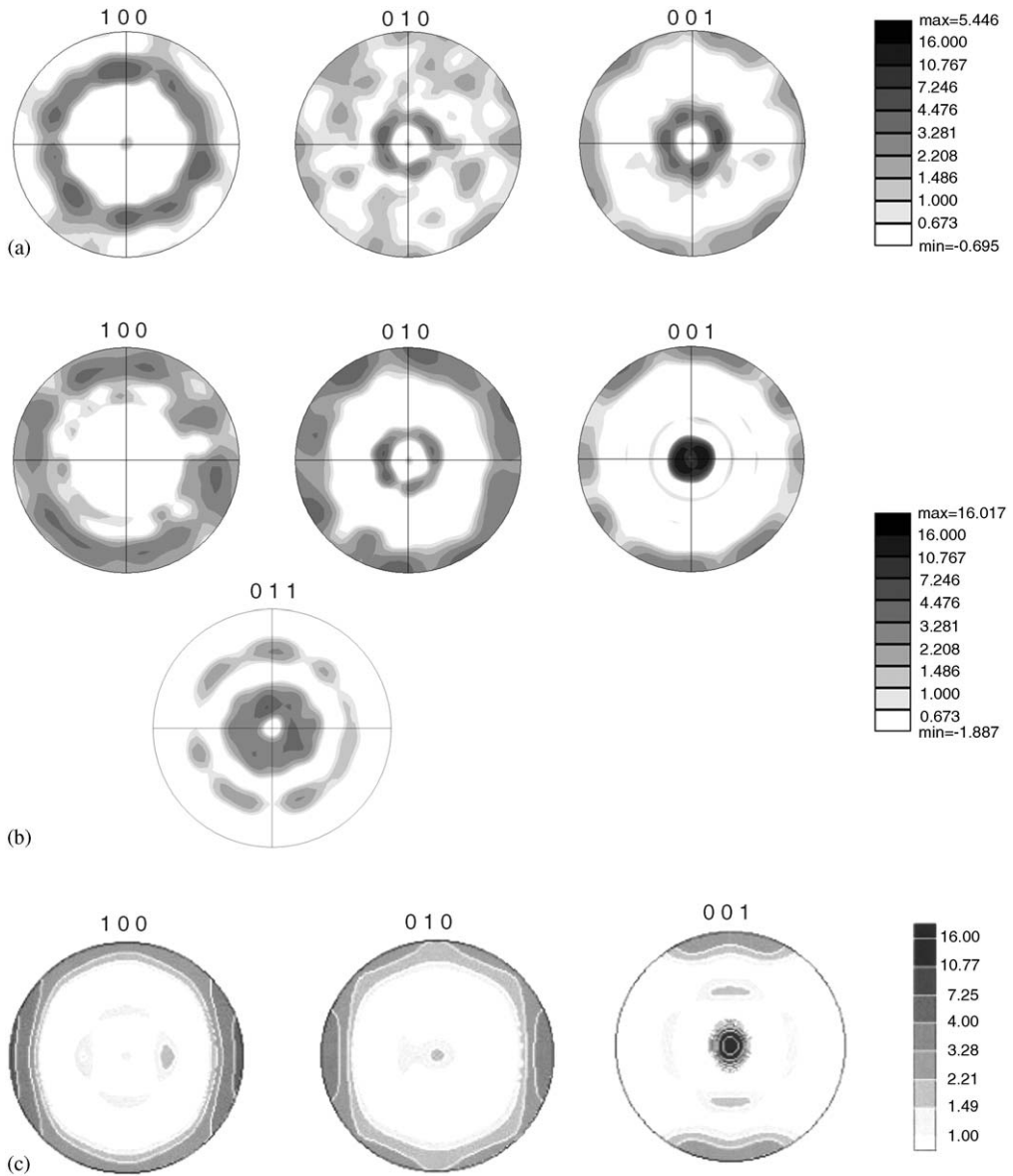
Fig. 8. Predicted and experimental pole figures in uniaxial tension: (a) predicted at $\bar{\varepsilon}_{eq} = 0.8$; (b) predicted at $\bar{\varepsilon}_{eq} = 2.1$; (c) experimental for a sample allowed to relax after a strain $\bar{\varepsilon}_{eq} = 2.1$ (Li et al., 2001). The tensile direction is normal to the equator plane of the figure.

4.4. Simple shear

Finally, we simulate simple shear of HDPE at a constant nominal shear rate $\dot{\bar{\gamma}} = 10^{-3}\,\text{s}^{-1}$. In the experiments of Dahoun (1992) and Bartczak et al. (1994), the applied nominal shear stress $\bar{\tau}$ and the nominal shear strain $\bar{\gamma}$ were measured. The model
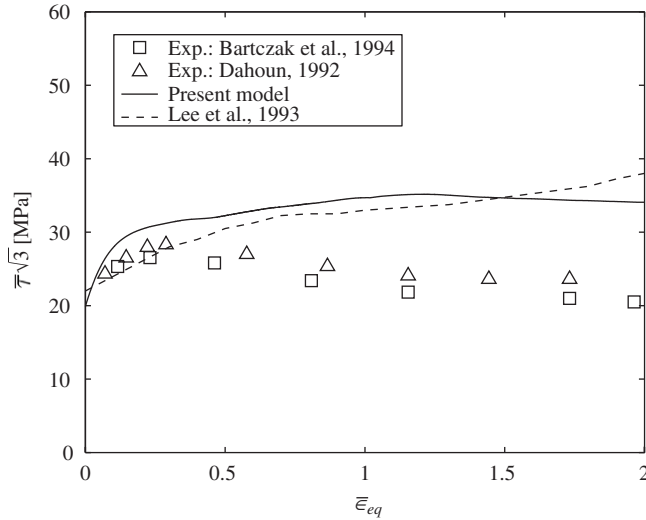
Fig. 9. Predicted and measured stress–strain curves for HDPE in simple shear.

predictions for the equivalent shear stress, $\overline{\tau}\sqrt{3}$, versus the equivalent strain, $\overline{\varepsilon}_{eq} = \overline{\gamma}/\sqrt{3}$, are compared to the experiment in Fig. 9. In the following, we do not discuss the normal stress difference related to simple shear because it has not been experimentally measured.

In this case, despite the differences between our model and the model of Lee et al. (1993a, b), the obtained results are very similar over the entire deformation range. Both models overestimate the stress at strains $\overline{\varepsilon}_{eq} > 0.3$. At strains $\overline{\varepsilon}_{eq} > 1.2$, our model predicts a slight strain softening whereas Lee et al. (1993b) obtain minor strain hardening. The discrepancy between the predicted and the measured stress may be due to several reasons. Firstly, it is very difficult to experimentally obtain simple shear deformation because shear experiments are accompanied by stress triaxiality and unloading effects near the sample ends. In fact, the normal stresses developing during large shear have not been measured in the experiments performed by Dahoun (1992) and Bartczak et al. (1994), which can partly explain the lower value of the measured equivalent stress. On the other hand, local drawing of material from the shoulders into the gauge section of the specimen (Lee et al., 1993a; Bartczak et al., 1994) is not taken into account in our simulation because the boundary conditions are applied to a single representative volume element. Better results for the stress–strain behavior in simple shear can be eventually obtained after integration of the micromechanical model in a finite element code and a full-scale modeling of the 3D sample geometry with more realistic boundary conditions.

The relative activity of the different deformation modes in function of $\overline{\varepsilon}_{eq}$ is shown in Fig. 10. Interestingly, the simulated activity of the modes strongly resembles that obtained in uniaxial tension, except the somewhat steeper decrease of the interlamellar shear rate and its earlier locking. At large shear strains, chain slip is by far the most active deformation mode.

The absence of macroscopic hardening in simple shear can be explained as follows: with increasing shear strain, the chain direction **c** rotates towards the shear direction. Because the crystals' resistances do not exhibit strain hardening and the imposed shear is
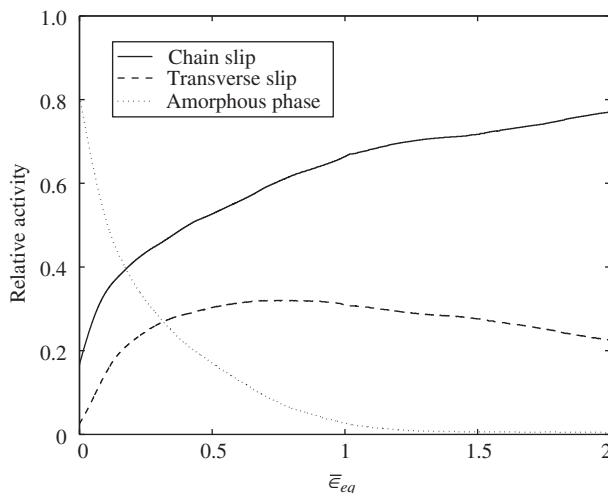
Fig. 10. Relative activity of the principal deformation modes in the phases vs. $\bar{\varepsilon}_{eq}$ in simple shear.

accommodated mostly by chain slip, the overall stress–strain curve remains flat despite the amorphous phase locking at large strains. Similar interpretation has been given by Parks and Ahzi (1990).

The predicted and experimental texture evolution in simple shear are compared in Fig. 11. The pole figures are plotted in stereographic projection. Upon increasing strain, the chain axes **c** cluster towards the direction of maximum stretch and rotate with it tending to align with the shear direction. The **a** axes follow a similar evolution pattern with their orientation fixed at 90° with respect to the **c** axes at all strains. The **b** axes develop a (0 2 0) component along the neutral direction. The (1 1 0) planes develop a weaker component oriented perpendicular to the maximum stretch that follows its strain-induced rotation and have a characteristic forked-tongue shape.

It is seen that our predictions are in good agreement with all experimentally observed characteristics of the texture evolution in simple shear, except the slightly sharper-than-observed development of the (2 0 0) and (0 0 2) textures. This can be explained by the fact that our predictions are for texture evolution during deformation while the experimental results are taken from relaxed samples. Consequently, the viscoelastic component of the mechanical behavior (implicitly taken into account in our simulations) influences, to some extent, the predicted texture while it has been relaxed in the measured samples. On the other hand, the predicted sharper texture is consistent with the overestimation of the shear stress at large strains, as it has already been discussed.

4.5. Morphology evolution

The influence of the morphology evolution on the stress–strain curves in uniaxial tension and compression is shown in Fig. 12. The difference between the stress–strain curves obtained with spherical inclusions and inclusions with a continuously evolving shape according to Eq. (31) is due to the dependency of the Eshelby tensor on the inclusions' shape in Eqs. (24) and (25). This in turn affects the estimation of the overall properties.
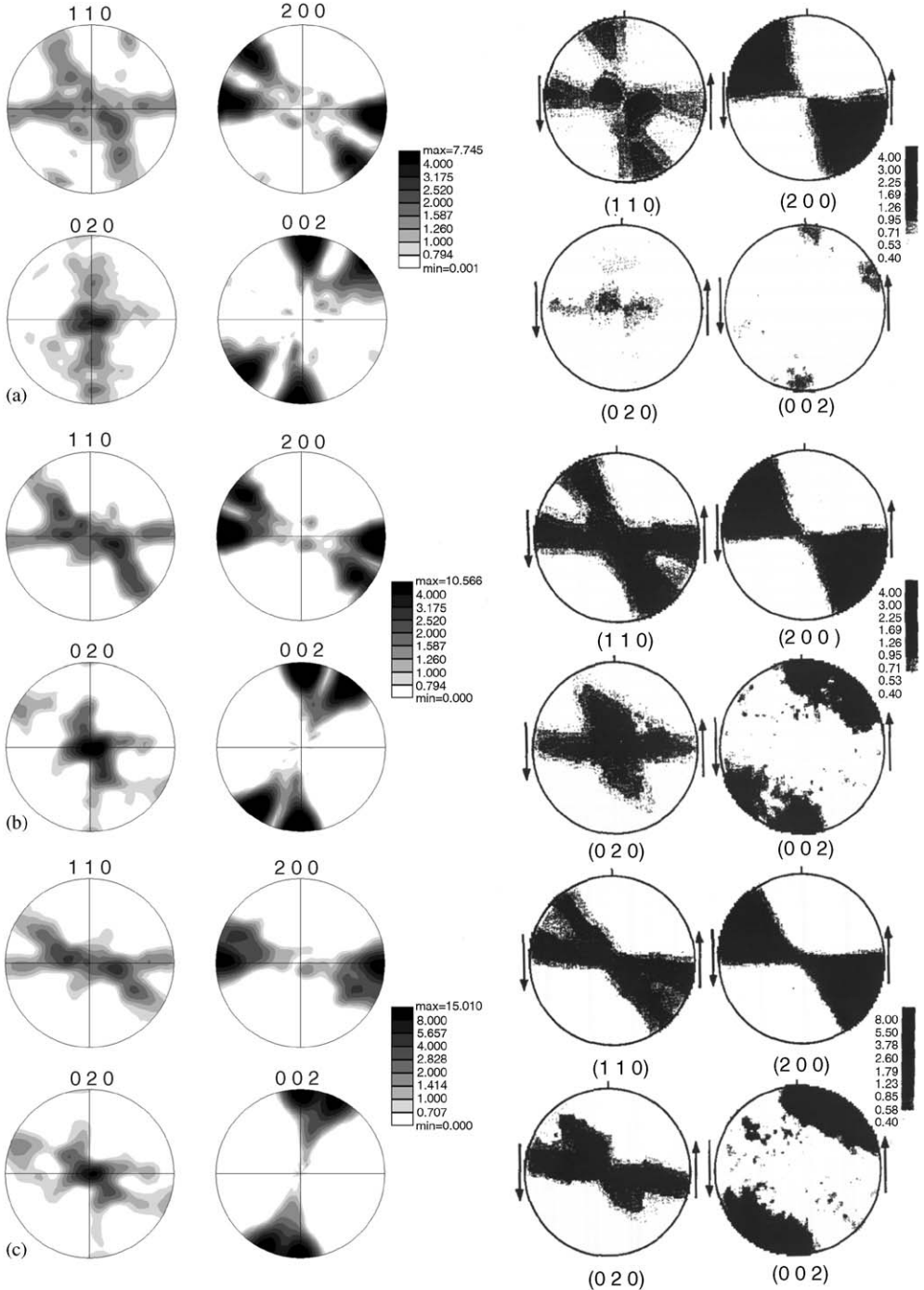
Fig. 11. Pole figures in simple shear at strains; (a) $\bar{\gamma} = 1.0$; (b) $\bar{\gamma} = 1.8$; (c) $\bar{\gamma} = 3.0$. Left: predicted; Right: experimental data after Bartczak et al. (1994). Arrows indicate the shear direction. The neutral direction is normal to the equator plane of the pole figure.
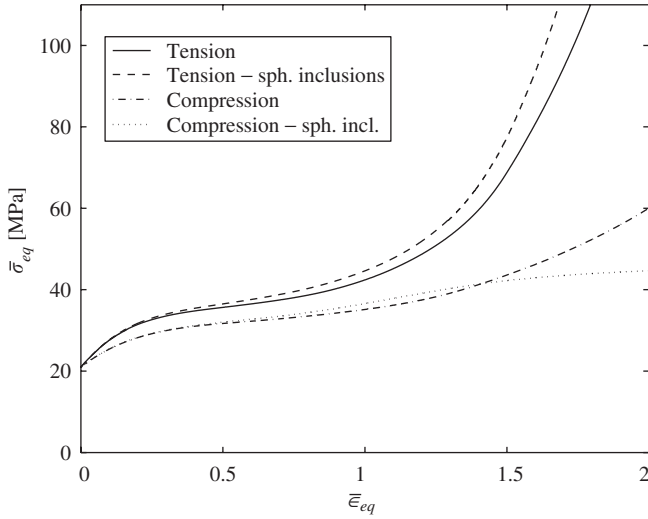
Fig. 12. Influence of the inclusions' shape evolution on the stress–strain behavior in uniaxial tension and compression.

Fig. 12 suggests that, without taking into account the morphology (inclusions' shape) evolution, it may be impossible to match the experimentally observed strain hardening in both tension and compression. In fact, the curves obtained with spherical inclusions in Fig. 12 are very close to the results reported in Lee et al. (1993a). In their subsequent work, Lee et al. (1993b) reduced the number of rigid links N for the amorphous phase chains from 49 to 12 in order to better fit the experimental stress–strain curve in compression. This resulted in a corresponding increase in the hardening of the predicted curve in tension, shifting the already stiff stress–strain response further away from the experimental data.

The evolution of the average inclusions' shape in uniaxial tension and compression is given in Fig. 13. In tension, the inclusions evolve into prolate ellipsoids with very high aspect ratio along the tensile axis at $\bar{\varepsilon}_{eq} \approx 2$. This mimics the strain-induced transition of the microstructure from lamellar to fibrillar.

In compression, the inclusions transform into oblate ellipsoids with their short axis aligned with the compressive direction. The shape evolution is noticeably less pronounced than in tension and resembles the evolution of the long period of the microstructure measured along and perpendicular to the compressive direction by Bartczak et al. (1992a).

The predicted morphology changes in simple shear with increasing $\bar{\gamma}$ are shown in Fig. 14. For concreteness, let us assume that the macroscopic shear proceeds along the $\mathbf{e}_1$ direction of a $\mathbf{e}_1 \otimes \mathbf{e}_2$ slip system fixed to a laboratory Cartesian basis $(\mathbf{e}_1, \mathbf{e}_2, \mathbf{e}_3)$. Along $\mathbf{e}_3$ (neutral direction), the aspect ratio remains unchanged. In directions along and perpendicular to the maximum stretch λ_{max} in the $(\mathbf{e}_1, \mathbf{e}_2)$ plane, the shape evolution resembles to that simulated in tension, which is consistent with the experimental evidence for development of fibrillar microstructure in simple shear (Bartczak et al., 1994).

In addition to the shape evolution, simple shear causes rotation of the maximum-stretch axis of the inclusions from an initial angle of $45°$ with respect to the shear direction $\mathbf{e}_1$.
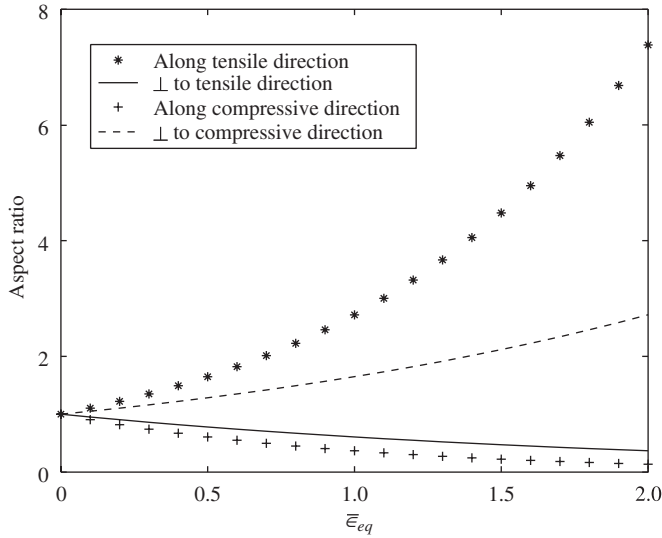
Fig. 13. Predicted evolution of inclusions' shape in uniaxial tension and compression.
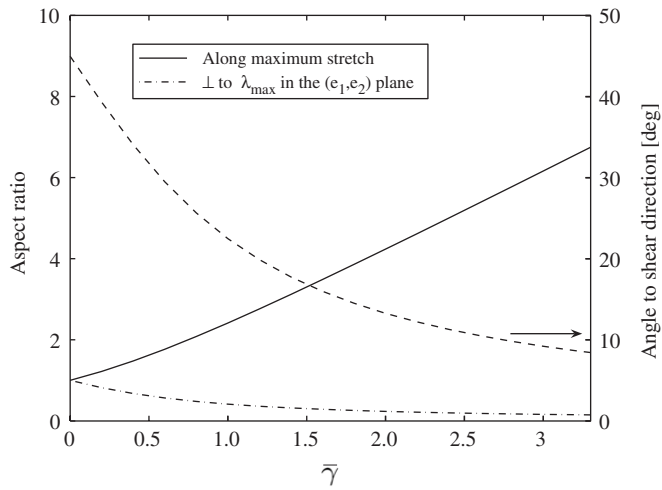
Fig. 14. Predicted evolution of the inclusions' shape and rotation of λ_{max} direction in simple shear.

With increasing strain, the direction of λ_{max} gradually aligns with the shear direction. The simulation results are given in the right-hand side of Fig. 14.

5. Conclusions

A micromechanical model for the large deformation behavior of semi-crystalline polymers has been developed and implemented. The model consists of three major parts: (i) constitutive equations for a composite inclusion comprising crystalline lamellae with their adjacent amorphous layers; (ii) a tangent self-consistent averaging scheme, and

(iii) an algorithm for strain-induced evolution of the inclusions' shape. The model predictions are in good agreement with virtually all aspects of the experimentally observed stress–strain behavior and texture evolution in HDPE in tension, compression and simple shear.

It has been shown that the morphology evolution and not the amorphous phase hardening determines the macroscopic strain hardening in uniaxial compression. Generally, the inclusions' shape evolution incorporated in the model provides an insight into the development of fibrillar morphology in uniaxial tension and simple shear but not in uniaxial compression.

In contrast to the bi-crystal approach of Lee et al. (1993a, b), we adopt single-crystal-like constitutive equations for the lamellae stacks where the amorphous phase shear is introduced as an additional slip system. The direct comparison between the two models shows that our model predicts the strain hardening in both uniaxial tension and compression better. In tension, a more realistic pace of texture development is obtained and the existence of the experimentally observed near-(0 1 1) and (0 1 0) components along the tensile axis is qualitatively predicted. In simple shear, both models give similar predictions for the stress–strain behavior and texture development and overestimate the observed shear stress. At this point, it is unclear whether this is due to the consideration of a single material point instead of the real 3D sample geometry or further modeling efforts are needed. A specific prediction of our model is the complete locking of the amorphous phase deformation at very large strains in all tested straining modes.

Acknowledgments

References

Ahzi, S., Parks, D.M., Argon, A.S., 1990. Modeling of plastic deformation evolution of anisotropy in semi-crystalline polymers. In: Singh, B. (Ed.), Computer Modeling and Simulation of Manufacturing Processes, ASME, MD-20, pp. 287–292.

Arruda, E.M., Boyce, M.C., 1993. A three-dimensional constitutive model for the large stretch behavior of rubber elastic materials. J. Mech. Phys. Solids 41 (2), 389–412.

Asaro, R.J., Needleman, A., 1985. Texture development and strain hardening in rate dependent polycrystals. Acta Metall. 33 (6), 923–953.

Bartczak, Z., Cohen, R.E., Argon, A.S., 1992a. Evolution of the crystalline texture of high-density polyethylene during uniaxial compression. Macromolecules 25, 4692–4704.

Bartczak, Z., Argon, A.S., Cohen, R.E., 1992b. Deformation mechanisms and plastic resistance in single-crystal-textured high density polyethylene. Macromolecules 25, 5036–5053.

Bartczak, Z., Argon, A.S., Cohen, R.E., 1994. Texture evolution in large strain simple shear deformation of high density polyethylene. Polymer 35 (16), 3427–3441.

Bassett, D.C., Hodge, A.M., 1981. On the morphology of melt-crystallized polyethylene I. Lamellar profiles. Proc. Royal Soc. London A 377, 25–37.

Butler, M.F., Donald, A.M., Ryan, A.J., 1998. Time resolved simultaneous small- and wide-angle X-ray scattering during polyethylene deformation—II. Cold drawing of linear polyethylene. Polymer 39 (1), 39–52.

Cohen, A., 1991. A Padé approximant to the inverse Langevin function. Rheol. Acta 30 (3), 270–273.

Dahoun, A., 1992. Comportement plastique et textures de déformation des polymères semi-cristallins en traction uniaxiale et cisaillement simple. Ph.D. Thesis, Institut national polytechnique de Lorraine.

Dahoun, A., Canova, G.R., Molinari, A., Philippe, M.J., G'Sell, Ch., 1991. Micromechanical modeling of the elasto—viscoplastic behavior of semi-crystalline polymers. Texture Microstruct. 14–18, 347–354.

Doghri, I., 2000. Mechanics of Deformable Solids: Linear and Nonlinear, Analytical and Computational Aspects. Springer, New York, pp. 381–383.

van Dommelen, J.A.W., Parks, D.M., Boyce, M.C., Brekelmans, W.A.M., Baaijens, F.P.T., 2003. Micromechanical modeling of the elasto–viscoplastic behavior of semi-crystalline polymers. J. Mech. Phys. Solids 51, 512–541.

Gautam, S., Balijepalli, S., Rutledge, G.C., 2000. Molecular simulations of the interlamellar phase in polymers. Effect of chain tilt. Macromolecules 33, 9136–9145.

G'Sell, C., Dahoun, A., 1994. Evolution of microstructure in semi-crystalline polymers under large plastic deformation. Mater. Sci. Eng. A 175, 183–199.

G'Sell, C., Jonas, J.J., 1979. Determination of the plastic behavior of solid polymers at constant true strain rate. J. Mater. Sci. 14, 583–591.

Hiss, R., Hobeika, S., Lynn, C., Strobl, G., 1999. Network stretching, slip processes, and fragmentation of crystallites during uniaxial drawing of polyethylene and related copolymers. A comparative study. Macromolecules 32 (13), 4390–4403.

Kok, S., Beaudoin, A.J., Tortorelli, D.A., 2002. A polycrystal plasticity model based on the mechanical threshold. Int. J. Plasticity 18 (5–6), 715–741.

Lebensohn, R., 1999. Modelling the role of local correlations in polycrystal plasticity using viscoplastic selfconsistent schemes. Model. Simul. Mater. Sci. Eng. 7, 739–746.

Lebensohn, R.A., Tomé, C.N., 1993. A self-consistent anisotropic approach for the simulation of plastic deformation and texture development of polycrystals: application to zirconium alloys. Acta Metall. Mater. 41 (9), 2611–2624.

Lebensohn, R.A., Tomé, C.N., 2003. Manual for code visco-plastic self-consistent (vpsc), version 6. Los Alamos National Laboratory, USA.

Lebensohn, R.A., Solas, D., Canova, G.R., Brechet, Y., 1996. Modeling damage of Al–Zn–Mg alloys. Acta Mater. 44, 315–325.

Lee, E.H., 1969. Elastic–plastic deformation at finite strains. J. Appl. Mech.: Trans. ASME 36, 1–6.

Lee, B.J., Parks, D.M., Ahzi, S., 1993a. Micromechanical modeling of large plastic deformation and texture evolution in semi-crystalline polymers. J. Mech. Phys. Solids 41 (10), 1651–1687.

Lee, B.J., Argon, A.S., Parks, D.M., Ahzi, S., Bartczak, Z., 1993b. Simulation of large strain plastic deformation and texture evolution in high density polyethylene. Polymer 34 (17), 3555–3575.

Li, D., Garmestani, H., Kalidindi, S.R., Alamo, R., 2001. Crystallographic texture evolution in high-density polyethylene during uniaxial tension. Polymer 42, 4903–4913.

Lin, L., Argon, A.S., 1994. Structure and plastic deformation of polyethylene. J. Mater. Sci. 29, 294–323.

Molinari, A., Canova, G.R., Ahzi, S., 1987. A self consistent approach of the large deformation polycrystal viscoplasticity. Acta Metall. 35 (12), 2983–2994.

Nikolov, S., Doghri, I., 2000. A micro/macro constitutive model for the small-deformation behavior of polyethylene. Polymer 41 (5), 1883–1891.

Nikolov, S., Doghri, I., Pierard, O., Zealouk, L., Goldberg, A., 2002. Multi-scale constitutive modeling of the small deformations of semi-crystalline polymers. J. Mech. Phys. Solids 50, 2275–2302.

Parks, D.M., Ahzi, S., 1990. Polycrystalline plastic deformation and texture evolution for crystals lacking five independent slip systems. J. Mech. Phys. Solids 38, 701–724.

Raabe, D., Chen, N., Chen, L., 2004. Crystallographic texture, amorphization, and recrystallization in rolled and heat treated polyethylene terephthalate (PET). Polymer 45 (24), 8265–8277.

Schultz, J., 1974. Polymer Materials Science. Prentice-Hall, Englewood Cliffs, NJ, USA.

Walpole, L.J., 1969. On the overall elastic moduli of composite materials. J. Mech. Phys. Solids 17, 235–251.